Journal of Power Sources 196 (2011) 361–370

Contents lists available at ScienceDirect

Journal of Power Sources

journal homepage: www.elsevier.com/locate/jpowsour

Continuum and atomistic models of strongly coupled diffusion, stress, and solute concentration

Hamed Haftbaradaran, Jun Song, W.A. Curtin, Huajian Gao*

School of Engineering, Brown University, Providence, RI 02912, USA

ARTICLE INFO

Article history:
Received 25 May 2010
Received in revised form 23 June 2010
Accepted 23 June 2010
Available online 30 June 2010

Keywords:
Diffusion-induced stress
Atomistic simulations
Stoichiometric limit
Activation energy
Binding energy

ABSTRACT

Poor cyclic performance of electrodes in lithium-ion rechargeable cell batteries is calling for efforts to develop continuum models of diffusion under very large stresses and high solute concentrations. The present work is aimed to develop such a model based on input from atomistic simulations. We consider four fundamental features of highly nonlinear behavior associated with diffusion at high solute concentrations. First, the effect of solute-induced stresses on the activation energy of solute diffusion could be important. Second, the solute concentration may be subject to an upper limit if there exists a stoichiometric maximum concentration. Third, the strong influence of the change in local chemical environment on the interaction energy between solute and host atoms could play a significant role. Fourth, we include the effect of the solute concentration on the Young's modulus of the host material. A continuum model is developed and validated based on atomistic simulations of hydrogen diffusion in nickel. The influences of each feature above are clearly discussed through parametric studies.

1. Introduction

Rechargeable battery cells have recently received much attention due to their broad potential applications in a variety of technologies including military, automobile, aerospace and medical industries [1,2]. Among various types of rechargeable batteries, lithium-ion (Li-ion) cells featuring higher energy capacity, higher operating voltage, lower self-discharge and lower maintenance requirement have become the most widely used secondary battery systems [3]. In the past, significant research has been directed toward increasing the charge and energy capacity of Li-ion batteries [1]. It has been shown that a noticeable increase in the charge capacity of batteries is achievable using Li-alloy (Li_XM; M = Sn, Si, Ge, Al) anodes [4]. Silicon (Si) possesses the highest known theoretical charge capacity (4200 mAh g^{-1}) corresponding to the formation of $Li_{22}Si_5$ but this capacity is accompanied by a 400% volume expansion [5]. Very large mechanical stresses associated with such a huge volume change during Li intercalation/deintercalation are responsible for poor cyclic behaviors of the Si anodes by inducing pulverization, fracture, loss of integrity and loss of electric contact with current collector. This major liability is obstructing the way toward widespread application of the Si anodes [2,6–11].

Much theoretical work has been devoted to continuum modeling of diffusion in battery electrodes. A number of continuum thermodynamics and kinetics models have been proposed in the literature such as the theory of porous electrodes [12,13] and the Dualfoil cell-sandwich model [14,15]. In addition, a large volume of publications has been devoted to the study of stress generation, deformation and fracture during diffusion. Study of diffusion-induced stresses based on an analogy with thermal stresses can be traced back to the work of Prussin [16]. The study was broadened to include the development of stresses during mass transfer in thin plates, solid cylinders and spheres, where the stress-diffusion coupling was considered by including the elastic inclusion energy of solute in the chemical potential [17–19]. During the past decade, an increasing number of continuum models of diffusion-induced stresses during charging/discharging of electrodes have been developed [20–26], some even accounting for the effects of surface tension and surface modulus [27–29]. Criteria for fracture in electrodes have also been discussed based on the maximum tensile stress criterion [22,23,25] and cohesive crack nucleation model [30].

Despite these developments, continuum models of diffusion under very large stresses and high solute concentrations usually face the challenge of strongly nonlinear system behavior. Validation of such models is often subject to limitations in experimental techniques. For instance, Christensen and Newman [22] presented an integrative model accounting for a number of different physical effects whose experimental validations are still lacking. Moreover, most of the existing models are either strictly applicable only in the limit of dilute concentrations [20,21,24,25] or do not account for non-conventional stress-diffusivity couplings

* Corresponding author.
E-mail address: Huajian_Gao@brown.edu (H. Gao).

0378-7753/$ – see front matter © 2010 Elsevier B.V. All rights reserved.
doi:10.1016/j.jpowsour.2010.06.080

that could be of importance for concentrated solutions and large stresses [22,23,26].

The aim of the present paper is to explore a simulation-based approach to developing continuum models of strongly nonlinear and coupled diffusion under very large stresses and high solute concentrations. Our model includes the effects of solute-induced stresses on the activation energy of solute diffusion, an upper limit for solute concentration, the interaction energy between solute and host atoms, as well as the effect of the solute concentration on the Young's modulus of the host material. On the other hand, we neglect the effects of surface tension and surface modulus [27–29] so that our model is really trying to capture the "bulk" behavior starting just inside the surface (associated with the flow of the material into the "bulk" due to an imposed flux at the "real" interface). In this way, our model is not a nanoscale model and has no special kinetics or energetics at the continuum surface. Although our atomistic simulations will be at nanoscale, the simulations are specially designed to avoid complications at a real electrolyte/material interface by artificially imposing an input flux inside the material just away from the outermost surface atomic layer, where bulk thermodynamics and kinetics applies (see more discussions later).

The paper is organized as follows. In Section 2, we introduce a continuum analytical model taking into account the four nonlinear features mentioned above. In Section 3, we discuss hydrogen in nickel as a test system to provide data against which the analytical model can be compared. The underlying material parameters needed in the continuum model are computed and the methods to accomplish direct molecular dynamics (MD) modeling of the charging of Ni by H at various rates are discussed. Section 4 contains our comparison of the analytical model against the MD, and demonstrates the role of the factors noted above in achieving quantitative predictions in the continuum model. We then investigate the influence of each individual physical effect on the overall charging process. A comparative study between the MD results and two versions of the classical models is also presented in Section 4. We conclude this section with a discussion on the applicability of the present model to the case of Li-ion batteries with Si anodes. A summary of our results is given in Section 5.

2. Continuum modeling of diffusion

For simplicity, consider one-dimensional diffusion in a plate under large stresses and high solute concentrations. We start by introducing a chemo-mechanical potential including the effect of high solute concentrations on the entropy of the system, the work required to insert an inclusion into an elastic matrix, and the concentration-dependent heat of solution. The diffusion-induced stresses are then presented for an infinitely extended free-standing plate using small-deformation theory, considering that the Young's modulus of the plate may vary with the solute concentration. We then introduce the stress-diffusivity coupling through the effect of internal stress field on the activation energy of diffusion. Finally, the generalized governing 1D diffusion equation is derived and the solution methodology is discussed.

2.1. Chemo-mechanical potential

To demonstrate the basic approach of simulation-based continuum modeling, we consider interstitial diffusion of solute atoms in a host solid. The interstitial sites of the host solid form a sublattice. With respect to this sublattice, the diffusion of the solute atoms can be viewed as a substitutional mechanism. The total number of interstitial sites in the original host lattice is assumed to be preserved.

In the continuum modeling of diffusion in solids, the drift velocity $\boldsymbol{v}$ and hence the flux of the diffusing species in the host material is given by [20,31,32]

$$J = cv = -Mc\nabla\mu^*, \tag{1}$$

where M is the mobility of the diffusing component, c is the solute concentration and μ^* is the chemo-mechanical potential incorporating the chemical and mechanical energies of the system. In the presence of internal stresses, the chemo-mechanical potential is expressed in terms of the chemical potential of the solute atoms μ_s and vacancies μ_v, partial molar volume of the solute Ω and the hydrostatic stress in the host solid σ_h as [32,33]

$$\mu^* = \mu_s - \mu_v - \Omega\sigma_h, \tag{2}$$

where

$$\mu_i = \mu_i^0 + RT\ \log a_i. \tag{3}$$

Here, $i \equiv s, v$ corresponds to the solute and vacancy components, respectively, μ_v^0 is the free energy of the host solid accommodating 1 mol of the vacant interstitial sites, μ_s^0 is the free energy of the same system when the interstitial sites are occupied by the solute atoms, R is the gas constant and T is the absolute temperature. The activity a_s accounts for the interaction energy between the host and solute atoms. A similar treatment of vacancies can be found in the thermodynamic description of adsorption equilibrium via vacancy solution theory [34,35], where activity of the vacancies is interpreted as the interaction between the adsorbate molecules and the host solid [36–38].

Recognizing the existence of a stoichiometric maximum concentration $c_{\max}$, activities of the components are related to their site fractions through $a_s = \gamma_s\tilde{c}$ and $a_v = \gamma_v(1-\tilde{c})$, where $\tilde{c} = c/c_{\max}$ and, γ_v and γ_s are the activity coefficients of the vacancies and solute atoms, respectively.

Therefore, the chemo-mechanical potential takes the following form:

$$\mu^* = \mu_0^{sv} + RT\log\frac{\tilde{c}}{1-\tilde{c}} - \Omega\sigma_h + RT\log\frac{\gamma_s}{\gamma_v}, \tag{4}$$

where $\mu_0^{sv} = \mu_0^s - \mu_0^v$ is a constant. Eq. (4) accommodates three important physical effects associated with high solute concentrations and large stresses as follows.

The second term on the right hand side of Eq. (4) is due to the entropy of a simple solution where the solutes occupy a fixed set of sites, such as interstitial or substitutional sites in the host material. For dilute solutions, where $\tilde{c} \ll 1$, this term reduces to the usual form $RT\log\tilde{c}$. However, the entropy of the system should reduce to zero as all the available sites in the host are filled with the solutes and so it is not possible to reach the saturation point. Introduction of this effect enables the present model to recognize a saturation limit for the host solid. Throughout this paper, this effect is referred to as the saturation effect.

The third term on the right hand side of Eq. (4) is the elastic energy associated with insertion of an inclusion of volume Ω into the matrix under the hydrostatic stress σ_h. This term was considered by Li [17], and is well-established in other contexts including diffusion around dislocations [39,40]. This effect is interchangeably referred to as the effect of hydrostatic stress or inclusion energy in the rest of this paper.

The last term on the right hand side of Eq. (4) represents the deviation of the solution behavior from an ideal solution which is ideal over the entire range of its composition [41]. This term reduces to a constant for dilute solutions and vanishes for an ideal solution. However, at high solute concentrations, the change in the chemical environment of the solution influences the interaction energy of the solute and host atoms. Since the activity coefficients γ_v and γ_s are related through the Gibbs–Duhem equation, they are determined based on the excess molar Gibbs free energy of the solution $G_{Ex}(\tilde{c})$ via $(\tilde{c}(1-\tilde{c})/RT)(d^2G_{Ex}/d\tilde{c}^2) = (\partial\log\gamma_s/\partial\log\tilde{c}) = (\partial\log\gamma_v/\partial\log$

$(1-\tilde{c})$), subject to the conditions $\gamma_s \to 1$ as $\tilde{c} \to 1$ and $\gamma_v \to 1$ as $\tilde{c} \to 0$. Therefore, one can simply verify that Eq. (4) can be rearranged in the following form:

$$\mu^* = \mu_0 + RT \log \frac{\tilde{c}}{1-\tilde{c}} - \Omega\sigma_h + \Delta\mu_0(\tilde{c}), \tag{5}$$

where $\mu_0 = \mu_0^{sv} + (dG_{Ex}(0)/d\tilde{c})$ is the chemical potential of an infinitely dilute solution, and $\Delta\mu_0(\tilde{c}) = (dG_{Ex}(\tilde{c})/d\tilde{c}) - (dG_{Ex}(0)/d\tilde{c})$ is the concentration-dependent binding energy between the solute particles and the host atoms as a function of the local concentration, which vanishes for an infinitely dilute solution. In the following section, we adopt the two-parameter Margules equation for the excess free energy of a binary solution [41],

$$G_{Ex}(\tilde{c}) = \tilde{c}(1-\tilde{c})[A_0\tilde{c} + B_0(1-\tilde{c})], \tag{6}$$

hence the concentration-dependent binding energy of the solution is given by

$$\Delta\mu_0(\tilde{c}) = 2(A_0 - 2B_0)\tilde{c} - 3(A_0 - B_0)\tilde{c}^2, \tag{7}$$

where A_0 and B_0 are the parameters of the Margules equation.

For an ideal dilute solution, where $\Delta\mu_0(\tilde{c}) = 0$ and $\tilde{c} \ll 1$, Eq. (5) reduces to the classical chemical potential [17–20].

2.2. Diffusion-induced stresses

Before proceeding to derive the generalized governing diffusion equation, we need to estimate the stress fields within the host solid. In this paper, we specialize the formulation to the case of an infinitely extended free-standing plate of width w subject to equal and uniform charging current densities on the side faces of the plate, as shown in Fig. 1.

The plate material is assumed to be an isotropic homogeneous linear elastic solid with Young's modulus E and Poisson's ratio ν. The Young's modulus of the material can be greatly affected as the solute concentration increases within the plate [42,43] and so here we explicitly consider a concentration-dependent Young's modulus $E(c)$. Following an analogy between thermal stresses and diffusion-induced stresses [16–21], the biaxial stress in the plate at position x through the plate thickness is given by

$$\sigma_b(x) = \sigma_{yy}(x) = \sigma_{zz}(x) = \frac{E\Omega}{3(1-\nu)}\left[\frac{(Ec)_{avg}}{E_{avg}} - c(x)\right], \tag{8}$$

where $(Ec)_{avg} = (1/w)\int_{-w/2}^{w/2} E(c(x))c(x)dx$, $E_{avg} = (1/w)\int_{-w/2}^{w/2} E(c(x))dx$ and hence $(Ec)_{avg}/E_{avg}$ is the modulus-weighted average concentration in the plate. We assume that the plate faces are traction-free and thus $\sigma_{xx} = 0$. Therefore the hydrostatic stress σ_h in the plate is two-thirds of the biaxial stress,

$$\sigma_h(x) = \frac{2E\Omega}{9(1-\nu)}\left[\frac{(Ec)_{avg}}{E_{avg}} - c(x)\right]. \tag{9}$$

2.3. Stress-dependent activation energy for diffusion

The diffusivity coefficient $\hat{D}$ is related to the mobility according to

$$\hat{D} = MRT. \tag{10}$$

Here we consider the effect of the internal stress field on the activation energy of diffusion, as follows. At the atomic scale, diffusion of a solute particle in a crystal lattice is described as a sequence of jumps from one interstitial site to an adjacent site, during which the diffusing particle must surmount the energy barrier caused by its interactions with the surrounding host atoms. Atomistic and quantum mechanical simulations have shown that this energy barrier

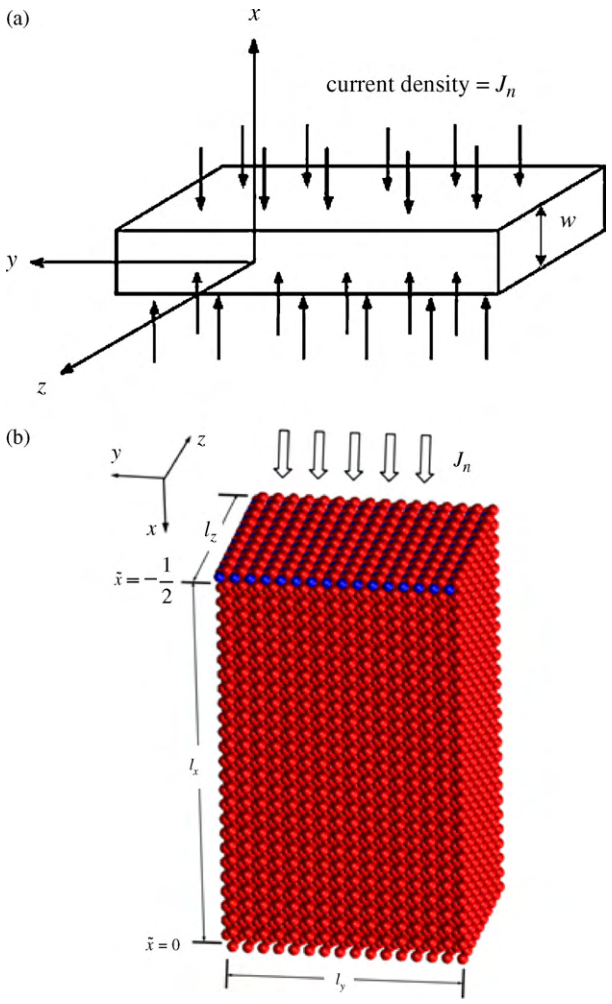

Fig. 1. A solid plate under atomic intercalation. (a) A plate of thickness w under uniform charging flux J_n on both of its faces. (b) The corresponding atomistic problem for H diffusion in Ni with the simulation cell being free along x-direction and periodic along y and z directions. During simulations, flux J_n of H atoms enter the simulation cell from the top surface while a reflecting boundary condition is imposed at the bottom surface.

is strongly affected by the internal stresses acting on the neighboring crystal atoms in the directions normal to the diffusion [44], suggesting a dependence on the biaxial stress. This effect has been referred to as strain-activated mobility by Aziz et al. [45–47] who showed that a stress-dependent mobility can cause a kinetically driven surface instability. Haftbaradaran et al. [48] found that the stress-mobility coupling can potentially lead to a surface locking instability in electrodes under galvanostatic intercalation.

Denoting the *change* in the activation energy due to the internal stresses as $\Delta E_b(\sigma_b)$, the diffusivity coefficient can be expressed as

$$\hat{D} = De^{-(\Delta E_b(\sigma_b))/RT}, \tag{11}$$

where D is the usual stress-free diffusivity. Normally, a tensile stress acting on the neighboring host atoms leads to a reduction in the energy barrier while a compressive stress increases it. Linearization of $\Delta E_b(\sigma_b)$ around the zero-stress value allows Eq. (11) to be written as

$$\hat{D} = De^{\alpha\Omega\sigma_b/RT}, \tag{12}$$

where α is a positive dimensionless coefficient. In the following section, we allow for a bilinear dependence of the activation energy on the biaxial stress and hence use $\alpha = \alpha_c$ for compressive stresses $\sigma_b < 0$ and $\alpha = \alpha_t$ for tensile stresses $\sigma_b > 0$. Aziz et

al. [45] have reported numerical values for the stress-diffusivity coupling through experimental measurements for the amorphous-crystalline interfacial growth of Si along [0 0 1] plane.

2.4. Generalized diffusion equation

With the chemo-mechanical potential, diffusion-induced stresses, and stress-diffusivity coupling given above, we can now develop the generalized diffusion equation for the simple case of a plate. We start with the fundamental diffusion equation given by

$$\frac{\partial c}{\partial t} + \nabla \cdot \boldsymbol{J} = 0, \tag{13}$$

where $\boldsymbol{J}$ is obtained using Eq. (1) and the chemo-mechanical potential μ^* is given in Eq. (5). Since the present problem is essentially one-dimensional along the x-direction, Eq. (13) with the aid of Eqs. (1), (5), and (10) takes on the following form:

$$\frac{\partial c}{\partial t} = \frac{\partial}{\partial x}\left[\hat{D}\left(\frac{c_{\max}}{c_{\max}-c}\frac{\partial c}{\partial x} - \frac{\Omega c}{RT}\frac{\partial \sigma_h}{\partial x} + \frac{c}{c_{\max}}\frac{1}{RT}\frac{d\Delta\mu_0(\tilde{c})}{d\tilde{c}}\frac{\partial c}{\partial x}\right)\right]. \tag{14}$$

Given the stress field in Eqs. (8) and (9) and the diffusivity $\hat{D}$ in Eq. (12), Eq. (14) can be cast into the dimensionless form:

$$\frac{\partial \tilde{c}}{\partial \tau} = \frac{\partial}{\partial \tilde{x}}\left[e^{k_1([\tilde{E}\tilde{c})_{avg}/\tilde{E}_{avg}]-\tilde{c})}\left(\frac{1}{1-\tilde{c}} + k_2\tilde{E}(\tilde{c})\tilde{c} - k_2\frac{d\tilde{E}(\tilde{c})}{d\tilde{c}}\left((\tilde{E}\tilde{c})_{avg}/\tilde{E}_{avg} - \tilde{c}\right)\tilde{c} + \tilde{c}\frac{d\Delta\tilde{\mu}_0(\tilde{c})}{d\tilde{c}}\right)\frac{\partial \tilde{c}}{\partial \tilde{x}}\right], \tag{15}$$

where $\tau = Dt/w^2$ is a dimensionless time, $\tilde{x} = x/w$ is the dimensionless length parameter, $\tilde{E}(\tilde{c}) = E(c)/E_0$ is the Young's modulus normalized with respect to the reference modulus E_0 at zero solute concentration, $\tilde{E}_{avg} = E_{avg}/E_0$ and $(\tilde{E}\tilde{c})_{avg} = (Ec)_{avg}/E_0 c_{\max}$. In Eq. (15), $k_1 = \alpha\Omega^2 E_0 c_{\max}/(3(1-\nu)RT)$ and $k_2 = 2\Omega^2 E_0 c_{\max}/(9(1-\nu)RT)$ are dimensionless parameters reflecting the stress-diffusion interactions, and $\Delta\tilde{\mu}_0(\tilde{c}) = \Delta\mu_0(\tilde{c})/RT$ is a dimensionless concentration-dependent binding energy. For a specified charging current density J_n at the plate faces $x = \pm w/2$, the required boundary conditions for Eq. (15) are

$$e^{k_1([\tilde{E}\tilde{c})_{avg}/\tilde{E}_{avg}]-\tilde{c})}\left(\frac{1}{1-\tilde{c}} + k_2\tilde{E}(\tilde{c})\tilde{c} - k_2\frac{d\tilde{E}(\tilde{c})}{d\tilde{c}}\left(\left[(\tilde{E}\tilde{c})_{avg}/\tilde{E}_{avg}\right] - \tilde{c}\right)\tilde{c} + \tilde{c}\frac{d\Delta\tilde{\mu}_0(\tilde{c})}{d\tilde{c}}\right)\frac{\partial \tilde{c}}{\partial \tilde{x}} = \pm\tilde{J}_n, \quad \tilde{x} = \pm 1/2 \tag{16}$$

where $\tilde{J}_n = J_n w/(FDc_{\max})$ is a dimensionless flux, with F being the Faraday constant. By comparison of Eq. (15) with the classical diffusion equation, one can define the effective diffusivity in the presence of all the aforementioned effects as

$$D_{eff} = De^{k_1([\tilde{E}\tilde{c})_{avg}/\tilde{E}_{avg}]-\tilde{c})}\left(\frac{1}{1-\tilde{c}} + k_2\tilde{E}(\tilde{c})\tilde{c} - k_2\frac{d\tilde{E}(\tilde{c})}{d\tilde{c}}\left(\left[(\tilde{E}\tilde{c})_{avg}/\tilde{E}_{avg}\right] - \tilde{c}\right)\tilde{c} + \tilde{c}\frac{d\Delta\tilde{\mu}_0(\tilde{c})}{d\tilde{c}}\right), \tag{17}$$

where $\tilde{c}$, and thus D_{eff}, is an implicit function of position x through the plate. A special case of Eq. (17) has been given by Wu [32].

2.5. Numerical solution methodology

The continuum model described above involves a highly nonlinear partial differential equation, Eq. (15), to be solved numerically under the boundary condition of Eq. (16) with zero initial concentration for Eq. (15). The governing equation is solved using FEMLAB (COMSOL Multiphysics) via the general PDE mode as

$$\frac{\partial \tilde{c}}{\partial t} + \nabla \cdot \boldsymbol{\Gamma} = 0, \tag{18}$$

with $\boldsymbol{\Gamma}$ defined as

$$\Gamma = -e^{k_1([\tilde{E}\tilde{c})_{avg}/\tilde{E}_{avg}]-\tilde{c})}\left(\frac{1}{1-\tilde{c}} + k_2\tilde{E}(\tilde{c})\tilde{c} - k_2\frac{d\tilde{E}(\tilde{c})}{d\tilde{c}}\left((\tilde{E}\tilde{c})_{avg}/\tilde{E}_{avg} - \tilde{c}\right)\tilde{c} + \tilde{c}\frac{d\Delta\tilde{\mu}_0(\tilde{c})}{d\tilde{c}}\right)\nabla\tilde{c}, \tag{19}$$

where coupling integration variables are used to define $\tilde{E}_{avg}$ and $(\tilde{E}\tilde{c})_{avg}$. Symmetry of the problem is invoked to solve the governing equation over half the domain, $0 \geq \tilde{x} \geq -0.5$, and 480 Lagrangian elements are used to discretize this domain. The Neumann boundary condition is applied at both boundary points with the flux $J_n = J_0(1-\tilde{c})$ at $\tilde{x} = -0.5$, designed to match the boundary condition in the molecular simulation (see next section), and zero flux at $\tilde{x} = 0$, consistent with the symmetry of the problem. Necessary material parameters for the model system of hydrogen charging of Ni are obtained from the atomistic models described in the next section.

3. Model validation via direct numerical simulation

To demonstrate the role played by the various physical phenomena associated with stress and solute concentration contained in the continuum model of Eqs. (15) and (16), here we consider a model material of hydrogen (H) solutes in a nickel (Ni) host. H in Ni provides a controlled system where H occupies well-defined sites in the host Ni lattice, the H-induced volume change is large enough to induce significant stresses, and the diffusion of H in Ni under stress is easily characterized. We use molecular statics and dynamics (i) to obtain the material parameters entering the continuum model and (ii) to explicitly model the charging of a Ni plate by an imposed flux of H atoms through the surfaces of the plate. We then compare the predictions of the continuum model to the molecular simulations.

3.1. Properties of H in Ni

We consider H in single crystal FCC Ni, using the interatomic embedded-atom-method [49,50] (EAM) potentials developed by Angelo et al. [51] to characterize the interactions between atoms in the system. At equilibrium, H atoms occupy octahedral sites in FCC Ni with a maximum attainable molar concentration $c_{\max} = 4/(N_A a_0{}^3)$ corresponding to the cubic hydride phase NiH, where N_A and a_0 are Avogadro's number and the Ni cubic cell lattice constant, respectively. The dimensionless concentration $\tilde{c} = c/c_{\max}$ is thus identical to the H/Ni ratio. The partial molar volume Ω, shown in Table 1 is determined by measuring the volume change of the system when H is introduced into the host at zero external pressure and zero temperature. The Reuss average elastic constants E_0, ν of the FCC Ni at zero temperature are also shown in Table 1. We neglect changes in the mechanical properties of the material as H is added to Ni by setting $\tilde{E}(\tilde{c}) = 1$ because Young's modulus for the fully hydrided NiH material is only about 10% larger than that of pure Ni. We have measured the concentration-dependent binding energy of the solution in eV atom^{-1} as $\Delta\mu_0(\tilde{c}) = -0.80\tilde{c} + 0.37\tilde{c}^2$ (which is identical to

Table 1
Numerical values of the model parameters.

Ω (m^3 mol^{-1})	$c_{\max}$ (mol m^{-3})	E_0 (GPa)	ν
2.053×10^{-6}	1.51×10^{-5}	205	0.31

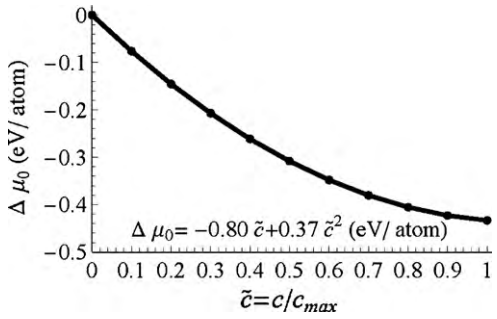

Fig. 2. Concentration-dependent binding energy $\Delta\mu_0$ as a function of $\tilde{c} = c/c_{\max}$ at 0 K.

the two-parameters Margules equation Eq. (7) with parameters $A_0 = 0.15$, $B_0 = 0.28$ in the same units), by creating a range of $NiH_{\tilde{c}}$ random solid solution materials and computing the energy per H atom. As shown in Fig. 2, the energy per H is increasingly negative with increasing $\tilde{c}$, favoring higher H concentrations, for this EAM potential. In particular at $\tilde{c} = 1$ (NiH), the current potential predicts unrealistic negative shear modulus, making it unsuitable to study system consisting of NiH. Nonetheless, in a forthcoming paper [52], it is shown that this problem can be fixed by adjusting some parameter in the original functional forms for the potential [51].

Diffusion of H in Ni occurs by H motion from one octahedral site to a neighboring site, corresponding to motion along the family of {1 1 0} directions in the fcc lattice. The activation energy E_b of H diffusion in the [1 1 0] direction under an applied uniaxial stress σ along $[1\,\bar{1}\,0]$ is computed using the nudged elastic band (NEB) method [53] with improved tangent calculation [54] and climbing procedure [55]. Using the activation energy under zero stress $E_b(0)$ as the reference value, we can compute $\Delta E_b(\sigma) = E_b(\sigma) - E_b(0)$. The results in Fig. 3 show that a tensile stress decreases ΔE_b while a compressive stress increases it. To conform to the simple continuum model of Eq. (12), we fit the simulation results to a bilinear curve to estimate the values of α under compression ($\alpha = \alpha_c = 0.180$) and under tension ($\alpha = \alpha_t = 0.404$). When no stress is present, $\Delta E_b = 0$ and the diffusivity is just D and is controlled by the zero-stress activation energy of 0.46 eV. Here, D at temperature T is calculated through direct MD simulations. We measure the hopping frequency Γ of a single H in an effectively infinite bulk Ni crystal under no external stresses and compute D as $D = \Gamma a_0^2/12$, neglecting correlation effects. Below, we study charging at T = 800 K to facilitate significant diffusion within the time constraints of molecular dynamics simulations, for which we calculate $D = 1.28 \pm 0.06 \times 10^{-9}\,m^2\,s^{-1}$. The diffusivity D estimated via other methods [56,57] using the activation energy under no stress (i.e., 0.46 eV [51]) gives results close to those we obtain from simulations.

3.2. Simulation of H charging of Ni

With the material system identified and characterized, we have performed a series of H-charging simulations using molecular dynamics (MD). The sample is a 1/2-plate geometry with simulation cell dimensions l_x = 6.2 nm, l_y = 4.0 nm and l_z = 3.6 nm, with the crystal orientation corresponding to $x = [1\,1\,0]$, $y = [1\,\bar{1}\,0]$, and $z = [0\,0\,\bar{1}]$ as shown in Fig. 1b. To mimic a semi-infinite plate in the lateral directions y and z, the simulation cell is periodic in these directions. To represent one-half of the full plate, charging occurs into the $\tilde{x} = -1/2$ surface and a symmetry boundary is used at $\tilde{x} = 0$. To create a system in which the charging rate can be controlled, and spurious effects associated with H on the Ni surface are avoided, we have designed special additional constraints as follows. To prevent H from exiting out of the system at $\tilde{x} = -1/2$ surface, which would be uncontrolled and energetically favorable due to the preference for H to reside on the Ni surface, we fully occupy the interstitial octahedral sites adjacent to the outermost layer of Ni atoms on the surface. This layer of H atoms and the neighboring uppermost layer of Ni atoms move together as a group in the x-direction and are expanded or contracted uniformly as a group via an affine transformation as the simulation cell dimensions change in y and z directions due to the charging (Fig. 1). In addition, a virtual reflection boundary is placed at the second row of Ni atoms such that the displacements and velocities of any H atom inside the plate trying to move through this virtual plane are reversed, preventing escape of H atoms. A similar virtual reflecting plane is imposed at $\tilde{x} = 0$ to enforce symmetry, and an additional layer of Ni atoms is placed adjacent to the $\tilde{x} = 0$ layer on the bottom to prevent surface effects. Aside from these constraints, all atoms are free to move.

The simulation temperature is fixed at 800 K using a Nosé–Hoover thermostat [58,59] and the simulation cell sizes in all directions fluctuate during the simulation using a barostat in order to maintain zero external pressure conditions [60,61]. The flux of H atoms is controlled by inserting H atoms at the desired rate J_0 into the layer of octahedral interstitial sites at $\tilde{x} = -1/2$ adjacent to the aforementioned fixed H atoms. To insert an H atom, one site, among the N = 160 possible sites in this layer, is chosen randomly for insertion at time intervals of $(\sqrt{2}N_A J_0 N a_0^2)^{-1}$ and an H atom insertion is attempted. If the chosen site is already occupied by an H atom, the insertion attempt is aborted. As H is inserted during charging, the concentration in the insertion layer increases due to insertion and decreases due to diffusion into the plate. The mean flux achieved in the simulation is then the desired flux multiplied by the probability of a successful insertion $(1 - \tilde{c}(\tilde{x} = -1/2))$ where $\tilde{c}(\tilde{x} = -1/2)$ is the surface concentration, or $J_n = J_0(1 - \tilde{c})\big|_{\tilde{x}=-1/2}$ (Fig. 1). Note that the actual influx is always subject to statistical fluctuations on top of the mean behaviors described above. The outcome of the simulation is the actual flux J_n as a function of time as well as the H concentration profile, defined as the average number of H atoms in the lateral cross-section at position x, as a function of time. The simulation results are converted into dimensionless quantities using the scalings identified in the development of the continuum model. Simulations are done at a number of charging rates, $\tilde{J}_0 = J_0 w/(FDc_{\max}) = 1.18, 5.89, 11.79, 117.9$. Fig. 4 shows the actual influx $\tilde{J}_n$ as a function of time for the above-mentioned values of the input flux. On the same figure, the predicted flux according to the approximation $\tilde{J}_n = \tilde{J}_0(1 - \tilde{c})\big|_{\tilde{x}=-1/2}$ is shown. Aside from the inevitable statistical fluctuations in the actual influx, Fig. 4 indicates that the above linear estimate is satisfactory for use in the continuum model.

Finally, we note that our simulations are designed to avoid complications due to kinetics and stresses at a real electrolyte/material interface, because we are interested here in the role of stress in controlling diffusion in the bulk of the material (that is, inside the material away from the immediate interface). Thus, our input flux is introduced inside the material just away from the (constrained) surface, where bulk thermodynamics and kinetics applies. In the simulation of nanoscale specimens, the surface stress arising from

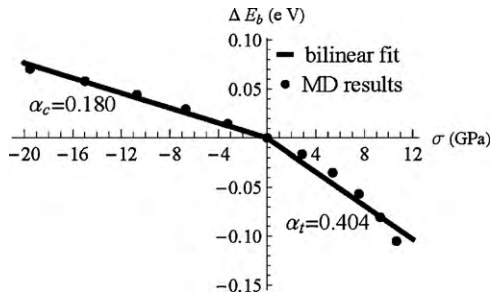

Fig. 3. Activation energy barrier of diffusion as a function of the normal stress acting perpendicular to the diffusion direction.

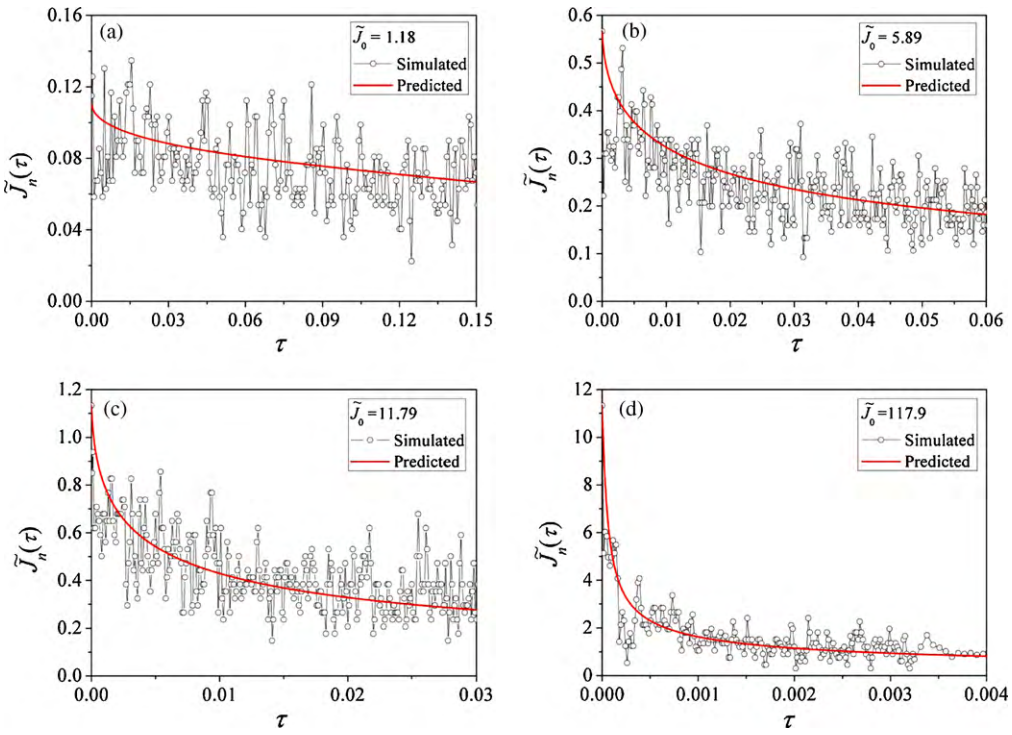

Fig. 4. Actual flux data versus the predictive relation as a function of time.

relaxation of the surface atoms can also generate internal stress in the "bulk" material of roughly $\sigma_{surface}(w_s/l_x)$ where $\sigma_{surface}$ is the surface stress and w_s an effective width of the surface layer. This induced stress is constant in the bulk, and thus generates no driving force for diffusion. However, this stress does affect the diffusion coefficient via Eq. (12). For our simulation sizes, with constraints on the surfaces as discussed above, the bulk biaxial pressure due to surface stresses is ~450 MPa (tension). This magnitude is small enough to be neglected (Fig. 3).

4. Results and analysis

The predictions of the H concentration profile through the plate at various times as obtained from the MD simulations and as predicted by the continuum model are shown in Fig. 5 for various charging rates $\tilde{J}_0 = J_0 w/(FDc_{\max}) = 1.18, 5.89, 11.79, 117.9$. In this figure, and in the rest of this paper, the atomic simulation results are shown as discrete points, corresponding to the average H concentration at each lateral octahedral site location x at each time, and

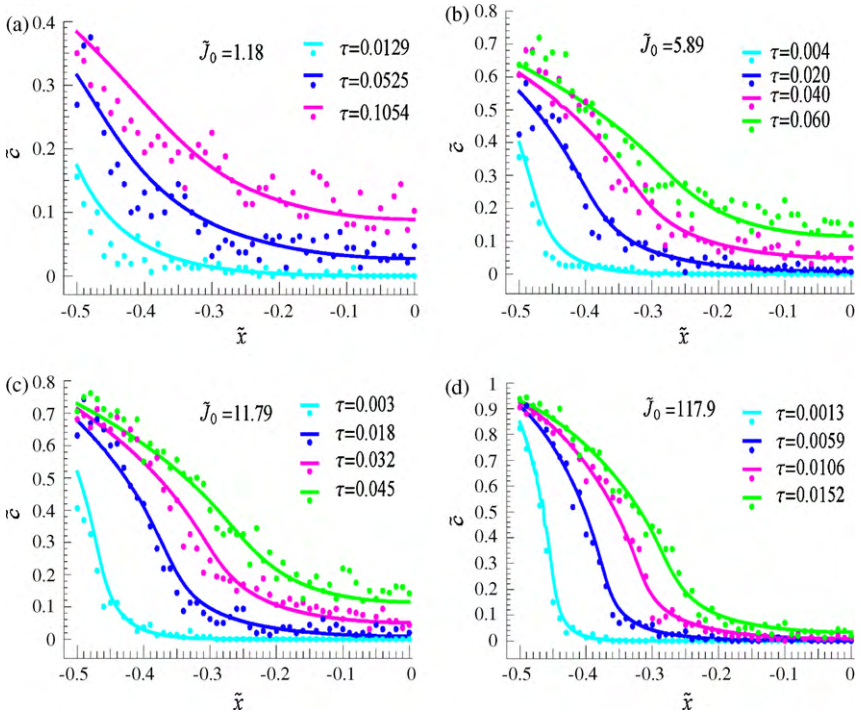

Fig. 5. Concentration profile across the thickness; dots are MD results and solid lines are the continuum model predictions.

the continuum predictions are shown as solid lines. For all charging rates and at all times shown, the continuum predictions are in excellent agreement with the MD results. This broad result validates the use of the continuum model for describing diffusion with strongly coupled stress effects.

As H is injected at the surface, the near-surface concentration rises, inducing a compressive stress in this region, which suppresses the H diffusivity in this region but also generates an energetic driving force for diffusion; see Eqs. (12) and (5). As the near-surface concentration increases further, with stress continuing to increase, the mean flux $J_n = J_0(1-\tilde{c})\big|_{\tilde{x}=-1/2}$ decreases and the surface concentration reaches a near-steady state value. At low flux levels, the surface concentration remains well below unity and the concentration profile is relatively smooth and convex. At high-flux levels, however, the surface concentration approaches unity and the concentration profile is concave and then convex, showing an inflection point. The flow of H into the plate resembles the motion of a diffuse interface.

We next scrutinize the individual contributions of stress-dependent activation energy, existence of a stoichiometric maximum limit, and the concentration-dependent heat of solution to the overall continuum model. To this end, limiting cases of the full model are considered in which one or more of the described physical effects are removed from the model while the others are preserved. In all subsequent figures, the simulation data remains unchanged from that shown in Fig. 5 since it is not possible to alter the characteristics of the physical system within the MD simulation.

4.1. Stress dependence of the activation energy

To assess the effect of stress-diffusivity coupling, the dependence of activation energy on stress is removed from the continuum model by considering the special case $k_1 = 0$ in Eq. (15), corresponding to setting the physical parameters $\alpha_c, \alpha_t = 0$. Fig. 6 shows the numerical results from the continuum model in comparison with the full MD results. In the absence of stress-diffusivity coupling, the diffusion coefficient near the plate surface, which is under compressive stress, is overestimated. Thus, more material is driven into the plate and the concentration profiles are overestimated in the interior regions. Also, as the charging flux increases, the effect of stresses on the energy barrier becomes more significant to the overall charging process.

4.2. Concentration dependence of the solute binding energy

The role of the concentration dependence of the binding energy in influencing the diffusion can be examined by setting $\Delta\tilde{\mu}_0(\tilde{c}) = 0$ in Eq. (15). Numerical results in this limit are shown in Fig. 7, where the predicted concentration profile is substantially more uniform than the full MD results. This is anticipated because the binding energy function prefers high H concentrations and so creates a driving force on the H atoms that acts in the opposite direction to the concentration gradient. Hence, when the binding energy is set to zero, the continuum model predicts a smoother concentration profile, as compared to the full problem. Fig. 7 thus reveals the pivotal role of this binding energy at high solute concentrations.

4.3. Effect of stoichiometric maximum limit

To examine the contribution of the "saturation cap" imposed by entropic considerations, this effect is removed from the continuum model by taking the dilute concentration limit, in which Eq. (15) (with $\tilde{E}(\tilde{c}) = 1$ for the Ni-H system), takes on the form:

$$\frac{\partial \tilde{c}}{\partial \tau} = \frac{\partial}{\partial \tilde{x}}\left[e^{k_1(\tilde{c}_{avg}-\tilde{c})}\left(1 + k_2\tilde{c} + \tilde{c}\frac{d\Delta\tilde{\mu}_0(\tilde{c})}{\partial \tilde{c}}\right)\frac{\partial \tilde{c}}{\partial \tilde{x}}\right]. \tag{20}$$

Eq. (20) clearly underestimates the effective diffusivity as compared to Eq. (15). This is particularly influential near the plate surface early in the charging process (not shown in Fig. 8) which leads to less solute in the system at later times. This results in underestimation of the concentration profiles at later times as shown in Fig. 8, mainly inside the material and for high fluxes. As well, the profiles obtained according to this model are sharper than those predicted by MD, which is directly related to the underestimation of the effective diffusivity.

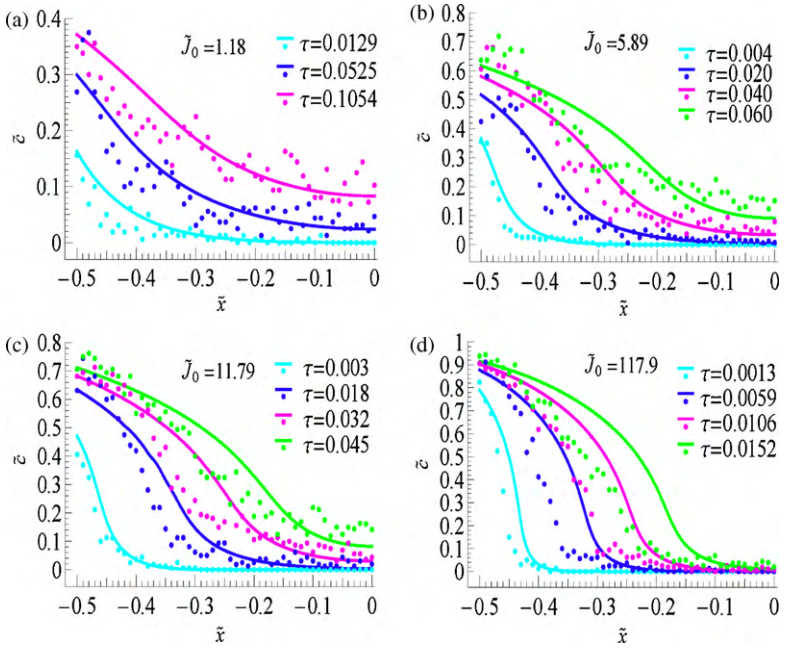

Fig. 6. Concentration profile across the thickness; atomistic simulation vs. continuum predictions neglecting the stress-diffusivity coupling.

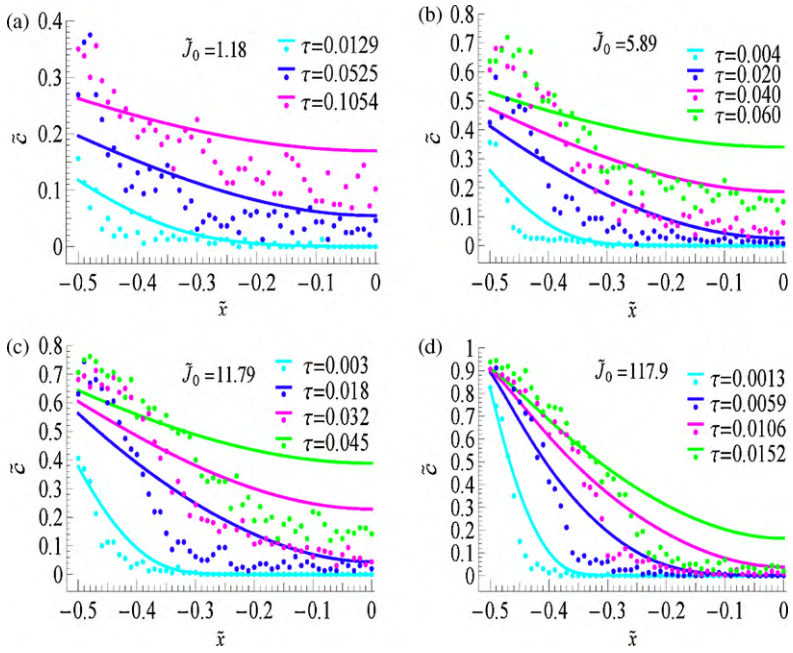

Fig. 7. Concentration profile across the thickness; atomistic simulation vs. continuum model neglecting the concentration dependence of the binding energy of the solution.

4.4. Comparison with the classical diffusion equations

In this section, two versions of the classical diffusion equations are employed to predict the concentration profile, and the results are compared with the MD results. In both models, the effects of stress-activation coupling, hydrostatic stress and concentration-dependent heat of solution are not included, i.e. $k_1 = k_2 = \Delta\tilde{\mu}_0(\tilde{c}) = 0$. In the first model, the saturation cap is not considered, and therefore Eq. (15) is reduced to

$$\frac{\partial \tilde{c}}{\partial \tau} = \frac{\partial^2 \tilde{c}}{\partial \tilde{x}^2}. \tag{21}$$

Concentration profiles as obtained according to this model are given in Fig. 9, together with the MD results. It should be noted that even though the saturation cap is not considered in this case, the charging flux decreases linearly to zero as the surface concentration tends to the saturation concentration. Hence, the concentration remains below the saturation concentration. A clear feature of the MD results which is not captured by this model is the emergence of the inflection point in the concentration profile. When the saturation cap is imposed in the classical model, the governing Eq. (15) is reduced to

$$\frac{\partial \tilde{c}}{\partial \tau} = \frac{\partial}{\partial \tilde{x}}\left(\frac{1}{1-\tilde{c}}\frac{\partial \tilde{c}}{\partial \tilde{x}}\right). \tag{22}$$

Fig. 10 compares the concentration profiles predicted by this model and the MD results. Although introduction of the saturation cap in the diffusion equation enables the model to capture

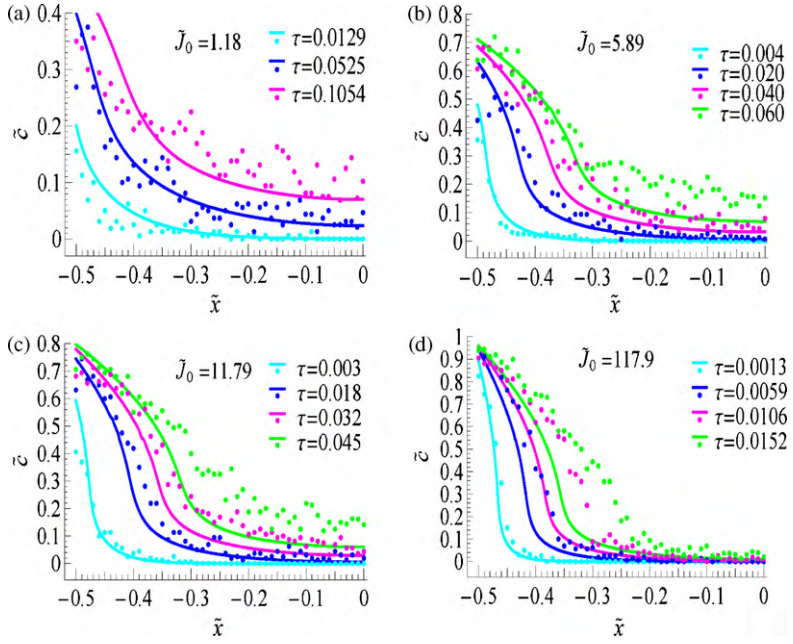

Fig. 8. Concentration profile across the thickness; atomistic simulation vs. continuum model without the saturation cap, Eq. (20).

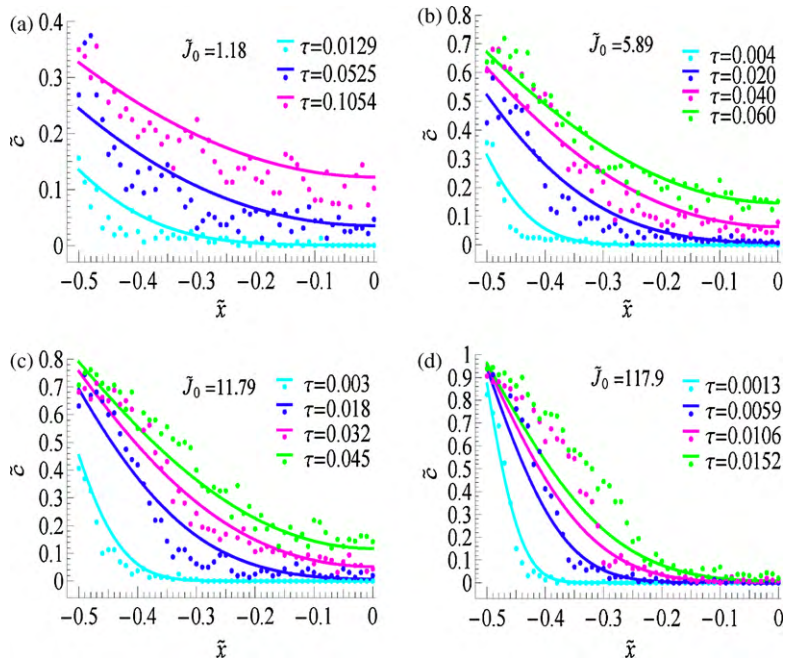

Fig. 9. Concentration profile across the thickness; atomistic simulation vs. classical model without saturation cap, Eq. (21).

the double-curvature behavior of the concentration profile, the figure shows the deviation of this model from the MD results. In particular, near the plate surface, the competition between the combined effect of the stress-dependent activation energy and the concentration-dependent heat of solution (both of which slow the diffusion) and the effect of the hydrostatic stress (which enhances the diffusion) is missing in this model. Fig. 10 indicates that in the regime of high charging rate the outcome is evidently an overestimation of the influx and hence the concentration profile.

According to Figs. 9 and 10, one could erroneously conclude that the classical diffusion equations are quantitatively satisfactory except for the highest flux case $\tilde{J}_0 = 117.9$, but this arises here only because of the cancellation of a number of independent competing effects. These effects do not necessarily cancel out in general. Even with significant cancellations in some regimes, Fig. 9 demonstrates that the classical diffusion equation fails in predicting the concentration profiles within the battery electrode for the high-flux charging regime of most practical importance. For other systems such as Li in Si, the physical effects described in this paper might come into play with different weights compared to H in Ni, highlighting one effect over the others.

4.5. Applicability and limitations for lithium diffusion in silicon

The present model is considered as an underlying framework for simulation of Li diffusion in Si. In this case, however, some additional complexities are important, including the structural change of the Si lattice resulting in amorphization. This would lead to an

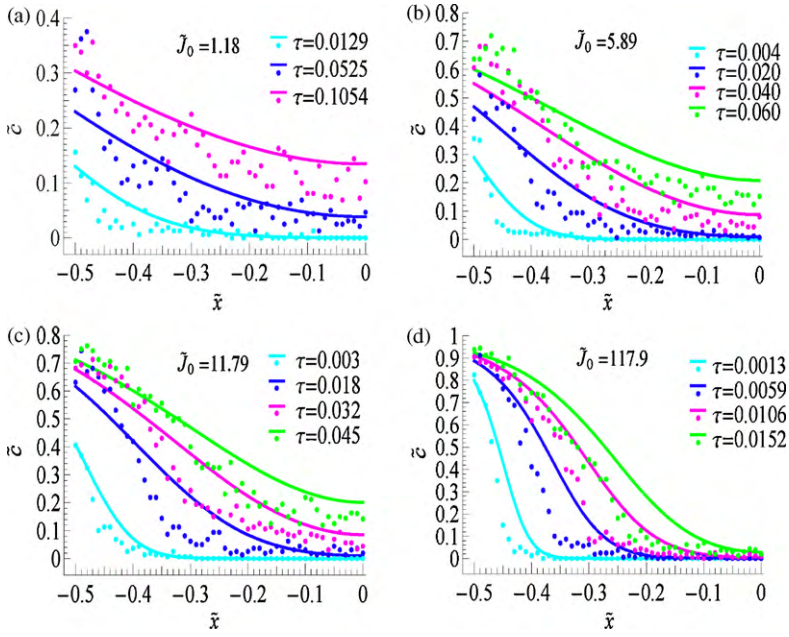

Fig. 10. Concentration profile, atomistic simulation vs. classical model with saturation cap, Eq. (22).

additional entropy in the system, emergence of inelastic behavior [62], and a strong influence on the partial molar volume of Li during intercalation/deintercalation. Furthermore, due to the 400% volume change arising during the cycling of Si, the deformation can easily exceed beyond the realm of small-deformation theory employed in the present model. However, the important nonlinear stress-diffusivity coupling considered here could be further highlighted for the Li/Si system, where huge deformation and large stresses are present. Furthermore, at high concentrations, the effect of solute saturation on the entropy of the system and that of the concentration-dependent binding energy should play substantial roles near the stoichiometric limit of the solution. Another feature of the Li/Si system that has been addressed in the present model is the change in the Young's modulus during intercalation. Although negligible for the case of hydrogen in nickel, the Young's moduli of Li-Si phases are greatly reduced relative to Si [42], even without amorphization.

5. Summary

A general continuum framework has been developed for modeling highly nonlinear behavior associated with atomic-scale diffusion at high solute concentrations and very large stresses. The continuum model introduces a new stress-diffusivity coupling through the effect of internal stresses on the activation energy of diffusion. The stoichiometric maximum concentration of the solute is explicitly recognized as the saturation limit by modifying the free energy of the system to account for high solute concentrations. The effect of the concentration-dependent binding energy between the host and solute atoms as a result of change in the chemical environment of the solution is accommodated. Finally, the mechanical properties of the host solid are also considered as a function of the solute concentration in the model.

The model was then validated for the case of hydrogen diffusion in nickel, and the continuum model predictions proved to be in excellent agreement with atomistic simulations. It was demonstrated that each of the above-mentioned effects, with the exception that change in mechanical properties of the host solid is negligible for the test system of this paper, plays a significant role in the overall predictions of the continuum model, especially at high charging rates. A comparative study between two versions of the classical diffusion equations and MD simulations was also presented. Capabilities and limitations of the continuum model for modeling diffusion of lithium in silicon anodes were discussed.

Acknowledgement

The work is supported by the GM-Brown Collaborative Research Laboratory on Computational Materials Science and the NSF MRSEC at Brown Grant No. DMR-0520651.

References

[1] U. Kasavajjula, C. Wang, A.J. Appleby, J. Power Sources 163 (2007) 1003–1039.
[2] C.K. Chan, H. Peng, G. Liu, K. McIlwrath, X.F. Zhang, R.A. Huggins, Y. Cui, Nat. Nanotechnol. 3 (2008) 31–35.
[3] J.M. Tarascon, M. Armand, Nature 414 (2001) 359–367.
[4] M.H. Kim, S.H. Ahn, J.W. Park, J.A. Ascencio, J. Korean Phys. Soc. 49 (2006) 1107–1110.
[5] B.A. Boukamp, G.C. Lesh, J. Huggins, J. Electrochem. Soc. 128 (1981) 725–729.
[6] M. Winter, J.O. Besenhard, M.E. Spahr, P. Novak, Adv. Mater. 10 (1998) 725–763.
[7] S. Bourderau, T. Brousse, D.M. Schleich, J. Power Sources 81 (1999) 223–226.
[8] M. Winter, J.O. Besenhard, Electrochim. Acta 45 (1999) 31–50.
[9] S.J. Lee, J.K. Lee, S.H. Chung, H.Y. Lee, S.M. Lee, H.K. Baik, J. Power Sources 97 (2001) 191–193.
[10] H.J. Ryu, J.W. Kim, Y.-E. Sung, S.M. Oh, Electrochem, Solid State Lett. 7 (2004) A306–A309.
[11] M. Yoshio, T. Tsumura, N. Dimov, J. Power Sources 146 (2005) 10–14.
[12] J. Newman, W. Tiedemann, AIChE J. 21 (1975) 25–41.
[13] R. Darling, J. Newman, J. Electrochem. Soc. 144 (1997) 4201–4208.
[14] M. Doyle, T.F. Fuller, J. Newman, J. Electrochem. Soc. 140 (1993) 1526–1533.
[15] T.F. Fuller, M. Doyle, J. Newman, J. Electrochem. Soc. 141 (1994) 1–10.
[16] S. Prussin, J. Appl. Phys. 32 (1961) 1867–1871.
[17] J.C.M. Li, Matall. Trans. A 9 (1978) 1353–1380.
[18] W.L. Wang, S. Lee, J.R. Chen, J. Appl. Phys. 91 (2002) 9584–9590.
[19] F. Yang, Mater. Sci. Eng. A 409 (2005) 153–159.
[20] X. Zhang, W. Shyy, A.M. Sastry, J. Electrochem. Soc. 154 (2007) A910–A916.
[21] X. Zhang, A.M. Sastry, W. Shyy, J. Electrochem. Soc. 155 (2008) A542–A552.
[22] J. Christensen, J. Newman, J. Solid State Electrochem. 10 (2006) 293–319.
[23] J. Christensen, J. Newman, J. Electrochem. Soc. 153 (2006) A1019–A1030.
[24] Y.-T. Cheng, M.W. Verbrugge, J. Power Sources 190 (2009) 453–460.
[25] Y.-T. Cheng, M.W. Verbrugge, J. Electrochem. Soc. 157 (2010) A508–A516.
[26] J. Christensen, J. Electrochem. Soc. 157 (2010) A366–A380.
[27] Y.-T. Cheng, M.W. Verbrugge, J. Appl. Phys. 104 (2008) 083521.
[28] M.W. Verbrugge, Y.-T. Cheng, ECS Trans. 16 (2008) 127–139.
[29] M.W. Verbrugge, Y.-T. Cheng, J. Electrochem. Soc. 156 (2009) A927–A937.
[30] T.K. Bhandakkar, H. Gao, Int. J. Solids Struct. 47 (2010) 1424–1434.
[31] W.R. McKinnon, R.R. Haering, in: R.E. White, J.O'M. Bockris, B.E. Conway (Eds.), Modern Aspects of Electrochemistry, Plenum Press, New York, 1983, No. 15.
[32] C.H. Wu, Int. J. Fract. 147 (2007) 227–234.
[33] J. Svoboda, F.D. Fischer, Acta Mater. 57 (2009) 4649–4657.
[34] S. Suwanayuen, R.P. Danner, AIChE J. 26 (1980) 68–76.
[35] S. Suwanayuen, R.P. Danner, AIChE J. 26 (1980) 76–83.
[36] L.P. Ding, S.K. Bhatia, Carbon 39 (2001) 2215–2229.
[37] L.P. Ding, S.K. Bhatia, Liu, Chem. Eng. Sci. 57 (2002) 3909–3928.
[38] S. Koter, A.P. Terzyk, J. Colloid Interface Sci. 282 (2005) 335–339.
[39] R.C. Picu, D. Zhang, Acta Mater. 52 (2004) 161–171.
[40] D.L. Olmsted, L.G. Hector Jr., W.A. Curtin, J. Mech. Phys. Solids 54 (2006) 1763–1788.
[41] J.M. Prausnitz, Molecular Thermodynamics of Fluid-phase Equilibria, Prentice-Hall, Englewood Cliffs, NJ, 1969.
[42] V.B. Shenoy, Y. Qi, P. Johari, J. Power Sources 195 (2010) 6825–6830.
[43] Y. Qi, H. Guo, L. G. Hector Jr., A. Timmons, Three-fold Increase in the Young's Modulus of Graphite Negative Electrode during Lithium Intercalation, Unpublished.
[44] L.D. Olmsted, R. Phillips, W.A. Curtin, Model. Simul. Mater. Sci. Eng. 12 (2004) 781–797.
[45] M.J. Aziz, P.C. Sabin, G.Q. Lu, Phys. Rev. B 44 (1991) 9812–9816.
[46] W.B. Carter, M.J. Aziz, Phys. Rev. Lett. 81 (1998) 1445–1448.
[47] P.W. Voorhess, M.J. Aziz, in: M.C. Smith, M.J. Miksis, G.B. McFadden, G.P. Neitzel, D.R. Canright (Eds.), Interfaces for the 21st Century, Imperial College Press, London, UK, 2002, pp. 167–176.
[48] H. Haftbaradaran, H. Gao, W.A. Curtin, Appl. Phys. Lett. 96 (091909) (2010) 1–3.
[49] M.S. Daw, M.I. Baskes, C.L. Bisson, W.G. Wolfer, in: R.H. Junes, W.W. Gerberich (Eds.), Modeling Environmental Effects on Crack Growth Processes, TMS-AIME, Warrendale, PA, 1986, pp. 99–124.
[50] S.M. Foiles, M.I. Baskes, M.S. Daw, Phys. Rev. B 33 (1986) 7983–7991.
[51] J.E. Angelo, N.R. Moody, M.I. Baskes, Model. Simul. Mater. Sci. Eng. 3 (1995) 289–307.
[52] J. Song, W.A. Curtin, A Nanoscale Mechanism of Hydrogen Embrittlement in Metals, Submitted.
[53] H. Jonsson, G. Mills, K. Jacobson, in: G. Berne, D. Coker, G. Cicotti (Eds.), Classical and Quantum Dynamics in Condensed Phase Simulations, World Scientific, Singapore, 1998, pp. 385–404.
[54] G. Henkelman, H. Jonsson, J. Chem. Phys. 113 (2000) 9978–9985.
[55] G. Henkelman, B.P. Uberuaga, H. Jonsson, J. Chem. Phys. 113 (2000) 9901–9904.
[56] A. Kimura, H.K. Birnbaum, Acta Metall. 36 (1988) 757–766.
[57] H. Mehrer, Diffusion in Solids: Fundamentals, Methods, Materials, Diffusion-Controlled Processes, Springer, New York, 2007.
[58] W.G. Hoover, Phys. Rev. A 31 (1985) 1695–1697.
[59] S. Nose, J. Chem. Phys. 81 (1984) 511–519.
[60] W.G. Hoover, Phys. Rev. A 34 (1986) 2499–2500.
[61] S. Melchionna, G. Ciccotti, B.L. Holian, Mol. Phys. 78 (1993) 533–544.
[62] V.A. Sethuraman, M.J. Chon, M. Shimshak, V. Srinivasan, P.R. Guduru, J. Power Sources 195 (2010) 5062–5066.